Flow induced deformation of vulnerable stenosis under pulsatile flow condition

Woorak Choi [1], Jun Hong Park,[1] Hojin Ha,[2] and Sang Joon Lee [1,*]

[1]*Department of Mechanical Engineering, Pohang University of Science and Technology (POSTECH), San 31, Hyoja-dong, Pohang 37673, Republic of Korea*
[2]*Department of Mechanical Engineering, Kangwon National University, Chuncheon, Republic of Korea*

A portion of vulnerable stenosis can be deformed periodically under pulsatile blood-flow condition. The deformable stenosis consists of fibrous cap covering a lipid pool, which is analogous to a capsule containing oily liquid or soft gel. The deformation increases mechanical stress acting on the fibrous cap. The magnitude of the stress determines likelihood of rupture, which causes sudden cardiac death or stroke. Previous studies tried to measure the stress by using intravascular imaging or numerical simulation. However, the methods have limitations of invasiveness and long process time in calculating the stress, respectively. In this study, the main determinants for the fibrous cap deformation and the normal stress acting on the fibrous caps are experimentally examined using deformable stenosis models. Particle image velocimetry is employed to measure flow induced forces acting on the fibrous caps. The deformable stenosis models are deformed to increase geometrical slope when inlet flow rate is increased. Deformation extent and mean normal stress acting on the fibrous caps are proportional to the square of the inlet flow rate and inversely proportional to the fibrous cap thickness. The periodic deformation of stenotic shape induces fluctuations of jet angle at the throat of the stenosis. Temporal variation of the jet angle is inversely proportional to the fibrous cap thickness of the deformable stenosis models. The variations of the jet angle for rigid stenosis models are negligibly small. The present results reveal the potential use of flow rate and variation of jet angle to approximate normal stress on the fibrous caps and to distinguish deformable stenosis from rigid stenosis. The flow rate and the jet angle can be measured directly by using noninvasive imaging devices in hospital.

I. INTRODUCTION

A vulnerable stenosis characterized by a relatively large lipid pool encapsulated with a fibrous cap is prone to rupture in the arteries [1]. Stenosis ruptures in coronary and carotid arteries cause 60–75% of sudden cardiac deaths [2] and strong strokes [3], respectively. A portion of vulnerable stenosis undergoes repeated shape deformation under a pulsatile blood-flow condition [4,5]. Clinical studies reported that patients with deformable stenosis repeatedly suffer from stroke [6,7]. Meairs and Hennerici [7] investigated deformation of stenosis in patients through follow-up study for 6 mo. They observed homogeneous surface motion with surrounding vessel walls near asymptomatic stenosis. However, they detected focal movement disparities near symptomatic stenoses. Huang *et al.* [8] reported that deformation of the carotid stenosis for patients with clinical symptom was larger than the deformation of the stenosis for asymptomatic patients.

---

*Corresponding author: sjlee@postech.ac.kr

043101-1

Current diagnostic strategies for the rupture mainly focus on geometrical features of vulnerable stenosis, including fibrous cap thickness and lipid pool size [9]. However, insufficient accuracy in the configuration-based diagnosis leads to studies on the underlying mechanism of stenotic rupture [10]. Stenotic rupture occurs when the mechanical stresses exerted on the fibrous cap exceed its own mechanical strength [11–13]. Normal stress acting on the cross sections of the thin fibrous cap dominantly affects the magnitude of resultant stress. The spatial distribution of the normal stresses can be obtained through numerical simulation to anticipate the rupture position [14–17]. Recent studies tried to utilize an intravascular ultrasound elastography to directly measure the normal stress on the fibrous cap, and the measurement accuracy was validated through *in vitro* experiments [18,19]. However, the numerical simulation and elastography have technical limitation in processing time and invasiveness, respectively.

The previous studies reported that the rupture was dominantly affected by pressure-induced normal stress, and the maximum normal stress was usually formed at the shoulder of the fibrous cap. However, roughly 40% of the rupture occur at other regions, including in the center of the cap in patients [20–22].

In this study, we investigated main determinant for the normal stress acting on the fibrous cap. We also tried to find a diagnosis index to distinguish the deformable stenosis from rigid stenosis, which can be measured in a simple and noninvasive manner. We focused on the effects of pressure nonuniformity instead of magnitude of pressure on the stress to explain the 40% rupture at other regions.

II. STENOSIS MODELS AND EXPERIMENTAL SETUP

A. Stenosis models

Three deformable and two rigid stenosis models were fabricated using Polydimethylsiloxane (PDMS, Sylgard 184, Dow Corning, Korea) material. Lipid pool-mimicking part (yellow color) was positioned in the upstream side of the deformable stenosis models as shown in Fig. 1(a). A rectangular PDMS film (4 mm × 8 mm) was placed between the lipid pool and the conduit [red film in Figs. 1(b) and 1(c)] to mimic a fibrous cap. Three deformable stenosis models have different film thicknesses ($h = 30 \pm 0.7$, 49 ± 1.3, and $139 \pm 2.5\,\mu m$), which were generated by regulating the rotational speed of a spin coater (SPIN30000, MIDAS, Korea) at 2500, 1500, and 500 rpm, correspondingly, for 1 min.

The two rigid stenosis models with different stenotic shapes [Fig. 2(c)] did not have the lipid pool to keep their stenosis shapes under two different pulsatile flow conditions [Fig. 2(a)]. The two rigid models have flat (flat-rigid) and curved (curved-rigid) upstream shapes as shown in Fig. 2(c). The deformable stenosis models have the same shape as the flat-rigid stenosis model before their deformations.

The models have an eccentric configuration with a 45% severity in inlet diameter ($D = 10\,mm$). Thus, the minimum diameter of the conduit is $0.55D$. The severities of many ruptured stenoses are lower than 50% [23]. Therefore, distinguishing the rupturable stenoses with severity smaller than 50% is strongly required. Detailed geometrical information is described in Appendix A.

The Young modulus (E) of the PDMS films was controlled to 39 ± 15 kPa by modulating the mixing ratio of the PDMS base to the curing agent (40:1), curing temperature (60 °C), and baking time (24 h) [24]. The E values of the human fibrous caps widely varied in the range of 40–20 000 kPa depending on their composition [25,26]. The rest of the model excluding the film was made of a stiff PDMS mixture (10:1, 65 °C, 1 h for $E = 2.61 \pm 0.021$ MPa) to minimize the deformation of the models. The temporal variation in the conduit diameter is less than 0.4%. The lipid pool was filled by a glycerol solution (47.38% distilled water, 36.94% glycerol, and 15.68% sodium iodine by weight) [27]. The glycerol solution was employed to mimic the kinematic viscosity ($\nu = 3.48 \times 10^{-6}$ m^2/s) of the blood and the refractive index ($n = 1.414$) of PDMS.
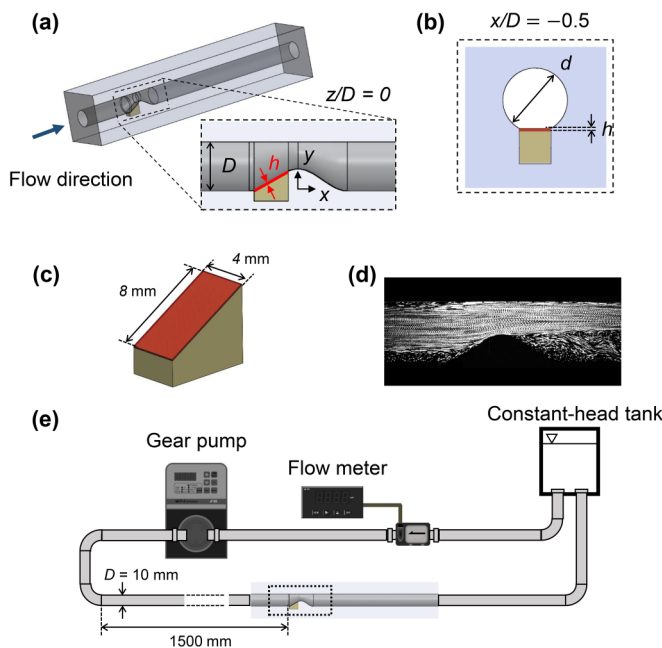
FIG. 1. (a) A schematic diagram of the deformable stenosis model (45% severity, diameter $D = 10\,\mathrm{mm}$) and a cross-sectional side view at the center plane ($z/D = 0$). A thin PDMS film (red line in the cross-sectional side view) is positioned between the lipid pool-mimicking part (yellow) and vessel conduit to mimic a fibrous cap. (b) Cross-sectional view of the deformable stenosis model at $x/D = -0.5$. (c) Configuration of the lipid pool-mimicking part and PDMS film (red color). (d) Path lines of a flow in the deformable stenosis model ($h = 30\,\mu\mathrm{m}$) at $t/T = 0.02$. Consecutive images obtained at $t/T = 0.02$ are stacked, and the maximum intensity at each pixel is projected. (e) Experimental setup including the flow circuit with a deformable stenosis model.

The three-dimensional (3D) molds of the conduit and the lipid pool were fabricated using a 3D printer (Fortus 400 mc, Stratasys) by using acrylonitrile butadiene styrene thermoplastic as a printing ink. After placing the prepared PDMS film at the interface between the two molds, 10:1 PDMS mixture was poured into the molds and baked in an oven. The mold of the lipid pool was gently pulled out through a slit through partial cutting. Thereafter, the PDMS mixture was poured on the slit to isolate the empty cavity. The glycerol solution was infused to fill the cavity. The embedded molds of the vessel conduit were pulled out after all the PDMS parts were cured. The two rigid stenosis models were fabricated using the 10:1 PDMS mixture only.

B. Flow circuit

Experiments were carried out in a closed loop of a pulsatile flow system, as illustrated in Fig. 1(e). A programmable gear pump (MCP-Z Process, Ismatec, Germany) was used to supply two different pulsatile flows [Fig. 2(a)], which provide similar waveforms as the real blood flow in the common carotid artery [28]. The mean Reynolds numbers (Re) of the two flow conditions are approximately 1000 (Q1) and 1300 (Q2) based on the inlet phase-averaged bulk velocity ($\tilde{U}_b$) and inlet diameter (D). The period (T) of the two pulsatile flows and the corresponding Wormesley number are 1 s and 6.72, respectively. The stenosis models were placed 150 D from the entrance of the conduit to secure a fully developed inlet flow [29]. The glycerol solution infused to mimic the lipid pool was also utilized as the working fluid. As tracer particles, fluorescence particles (FPP-RhB-35, Dantec Dynamics, Denmark) were used. The average diameter and density of the tracer particles were approximately $20-50\,\mu\mathrm{m}$ and 1.19 g/ml, respectively. A high-speed camera (FASTCAM SA1.1,
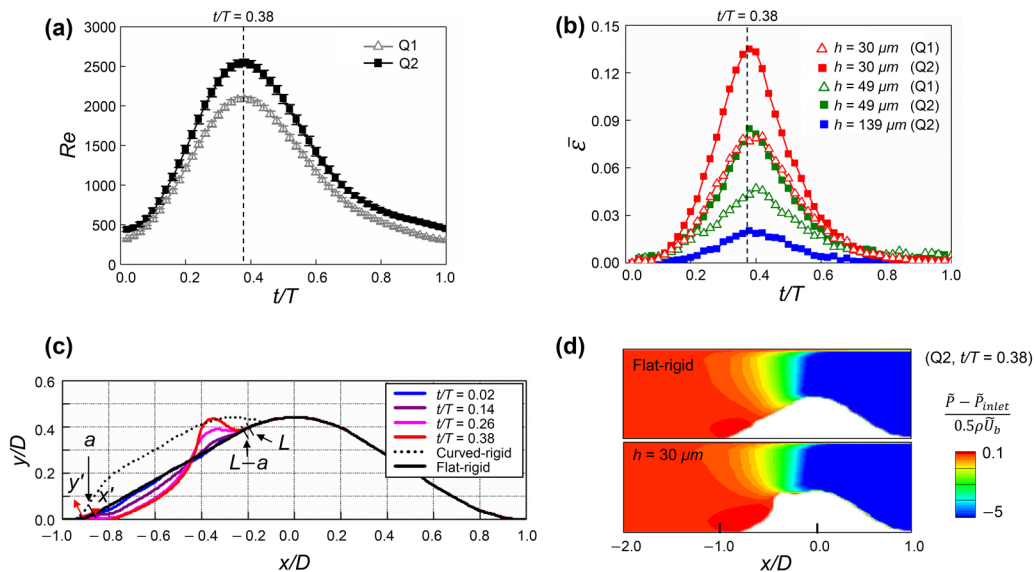
FIG. 2. Deformation of stenosis models. (a) Waveforms of the inlet Reynolds number (Re) based on D and the phase-averaged bulk velocity ($\widetilde{U}_b$). Error bars denote the standard deviation of the data collected from each experiment. (b) Variations of mean strain ($\bar{\varepsilon}$) acting on the PDMS film of each deformable stenosis model at the center plane ($z/D = 0$). (c) Temporal variation of the PDMS film of the deformable stenosis model ($h = 30\,\mu$m) at four different phases. The results for two rigid models at the center plane ($z/D = 0$) are compared. The rigid models are made of bulk PDMS to keep their shapes under pulsatile flow conditions. (d) Contour maps of nondimensional differential pressure around a flat-rigid and a deformable ($h = 30\,\mu$m) stenosis model at $t/T = 0.38$ under Q2 flow condition. Here, $\tilde{P}_{inlet}$ represents the phase-averaged pressure at inlet ($x/D = 2$).

Photron, Japan) was positioned perpendicular to the stenosis model to measure the velocity fields in the center plane ($z/D = 0$). The measurement plane was illuminated with a thin laser light sheet of 0.5 mm in thickness formed by a 1-W continuous laser (Shanghai Dream Lasers Technology Co., China).

C. Particle image velocimetry (PIV) analysis

A high-speed camera was employed to capture consecutive flow images with intervals of 1/8000 s. The camera was connected to a delay generator (575-8C, BNC, USA) to obtain 10,000 pairs of flow images for 10 cycles. A pair of images was acquired with intervals of 1/1000 s. The captured flow images were processed using the PIVVIEW software (PIVVIEW 2C, PIVTEC, Germany). Fast Fourier transform-based cross-correlation PIV algorithm was applied to consecutive flow images to obtain instantaneous velocity field information. A multigrid interrogation window scheme was adopted for interrogation windows of 64×64, 32×32, and 24×12 pixels with 50% overlapping. The horizontal and vertical distances between the two adjacent velocity vectors were 12 and 6 pixels, respectively. These vectors correspond to the physical dimensions of 0.48 and 0.24 mm. Each cycle was divided into 50 equally spaced phase bins (200 samples per bin) for phase-averaged evaluation. Uncertainty analysis was conducted by comparing the root-mean-square values of the fluctuating velocity components with varying the number of cycles. The error was converged to be smaller than 5%, as discussed in our previous study [30]. Pressure gradients were calculated from the PIV results. The values of pressure gradients were integrated from $x/D = -2$ by using the forward Euler spatial integration scheme to obtain pressure-field information, as illustrated in Fig. 2(d) [31].

The uncertainty of PIV measurements is relatively high in the near-wall region, due to high-velocity gradient in the region and difficulty of accurate wall detection [32]. To minimize such measurement error, the time interval between consecutive flow images ($=1/8000$ s) was adjusted to make displacement variation for tracer particles in an interrogation window be smaller than mean particle diameter [33]. In addition, the wall position was detected by using standard deviation values of light intensity in sequential flow images [34] and the detection was verified based on the conduit diameter ($=10$ mm). The difference in pressure values at the wall and adjacent interrogation window was smaller than 0.8% of the mean pressure difference along the wall, which was utilized as the main parameter for data analysis.

III. RESULTS AND DISCUSSION

A. Deformation of stenosis under pulsatile flow condition

The deformable stenosis models initially have the same shape as the flat-rigid stenosis model. However, the upstream configuration varies with the increase in flow rate as shown in Fig. 2(c). The length (L) variations of the PDMS films were measured at the center plane ($z/D = 0$) to evaluate the mean strain [$\bar{\varepsilon} = (L - L_{t/T=0.02})/L_{t/T=0.02}$]. The value of $\bar{\varepsilon}$ increases when the flow rate increases and the film thickness decreases as illustrated in Fig. 2(b). The maximum values of $\bar{\varepsilon}$ for Q2 conditions are approximately 65% larger than those for Q1 conditions for each model, although the maximum Reynolds number (Re) number has only ∼25% difference for the two different flow conditions [Fig. 2(a)]. The deformation of each cap film enclosing glycerol solution (lipid pool-mimicking part) mainly results from the static pressure nonuniformity acting on the film. The static pressure (P) gradually decreases when the flow velocity increases from $x/D = -1$ to $x/D = 0$ due to the reduction of conduit area as shown in Fig. 2(d). The films are deformed in downward and upward directions in the front and rear parts, respectively [Fig. 2(c)] because of relatively high and low static pressure in each position.

B. Mechanical stress on PDMS films

The relationship between pressure distribution on the film and its shape deformation was analyzed using the following membrane stress equation [35]:

$$\sigma_\theta/r_\theta + \sigma_\emptyset/r_\emptyset = (\widetilde{P_i} - \tilde{P})/h, \tag{1}$$

where r_θ, $r_\emptyset$, σ_θ, $\sigma_\emptyset$ indicate the radius of curvature in the local latitude and longitudinal planes and the normal stress on the cross sections acting on the local latitude and lgitudinal directions, respectively. Phase-averaged value of I was expressed by $\tilde{I}$ in the present study. In Eq. (1), $\widetilde{P_i}$ corresponds to the internal pressure of liquid in the lipid pool of the stenosis models. The variation of $\widetilde{P_i}$ in the lipid pool is assumed to be negligibly small comparing to the variation of pressure acting along the outside of the film ($\tilde{P}$). The value of $\widetilde{P_i}$ can be calculated from the spatial distribution of $\tilde{P}$ by using the force balance in the y' direction at a part of the film in the center plane [Fig. 2(c)] as follows:

$$\widetilde{P_i} = \frac{1}{L - 2a} \int_a^{L-a} \tilde{P} dx' + \frac{h}{L - 2a}(\sigma_{x'=a} \times \sin\beta_{x'=a} - \sigma_{x'=L-a} \times \sin\beta_{x'=L-a}), \tag{2}$$

where β indicates angle of the deformed film with the x' axis. The second and third terms on the right-hand side denote the normal stress exerting on the cross sections of the film at $(x', y') = (a, 0)$ and $(L - a, 0)$, where normal stress is much larger than the bending and shear stresses. The value of "a" can be approximated to "0" in the present condition because the deflection (w) of the film is much larger than its thickness (h) at most positions. Thus, the first term in the right-hand side can be approximated to $\frac{1}{L} \int_0^L \tilde{P} dx'$, which represents the mean pressure along the film at the center plane ($0 < x' < L$). The L value is fixed to 8 mm in the present stenotic model as shown in Fig. 1(c). The

TABLE I. List of representative parameters.

Symbol	Description	Symbol	Description
D	Inlet diameter of a conduit (characteristic length scale)	U	Time-averaged bulk velocity (characteristic velocity scale)
h	Thickness of PDMS films	$\tilde{U}_b$	Phase-averaged bulk velocity
$\tilde{P}$	Phase-averaged pressure	$\bar{w}$	Mean deflection of a film
$\widetilde{P}_i$	Phase-averaged internal pressure of liquid in the lipid pool	$\bar{\alpha}$	Mean angle of the velocity vector
$\Delta\tilde{P}_{\mathrm{film}}$	Phase-averaged magnitude of pressure nonuniformity at a film	$\bar{\varepsilon}$	Mean normal strain at a film
R	Inlet radius of a conduit	$\bar{\sigma}$	Mean normal stress at a film

normal stress acting on the film in the z' direction is negligibly small because the deformed shape is smooth and symmetric to the center plane ($\partial w/\partial z' = 0$).

The relationship between the pressure $\tilde{P}$ and strain ε can be derived by substituting Eq. (2) and Hooke's law for plane stress [36], $\sigma_{\theta,\emptyset} = E(\varepsilon_{\theta,\emptyset} + \nu\varepsilon_{\emptyset,\theta})/(1 - \nu^2)$, into Eq. (1).

$$\frac{\tilde{P} - \frac{1}{L}\int_0^L \tilde{P}dx'}{h} = -\frac{E}{1 - \nu^2}\left(\frac{\varepsilon_\theta + \nu\varepsilon_\emptyset}{r_\theta} + \frac{\varepsilon_\emptyset + \nu\varepsilon_\theta}{r_\emptyset}\right) + \frac{EK}{L(1 - \nu^2)}, \quad (3)$$

where K denotes $(\varepsilon_\theta + \nu\varepsilon_\emptyset)_{x'=a}\sin\beta_{x'=a} - (\varepsilon_\theta + \nu\varepsilon_\emptyset)_{x'=L-a}\sin\beta_{x'=L-a}$. The reported values of the Poisson's ratio ($\nu = 0.5$) and Young's modulus ($E = 39 \pm 15\,\mathrm{kPa}$) for the PDMS are utilized in this study [24,37]. To investigate the governing parameters that determine the stenotic deformation, we rearrange Eq. (3) and nondimensionalize geometrical indexes, $r_{\theta,\emptyset}$ and L, using diameter of the conduit (D).

$$\frac{(\tilde{P} - \frac{1}{L}\int_0^L \tilde{P}dx')D}{Eh} = -\frac{1}{1 - \nu^2}\left(\frac{\varepsilon_\theta + \nu\varepsilon_\emptyset}{r_\theta^*} + \frac{\varepsilon_\emptyset + \nu\varepsilon_\theta}{r_\emptyset^*}\right) + \frac{K}{L^*(1 - \nu^2)}, \quad (4)$$

where dimensionless variable I is expressed by I^* (see Table I). A nondimensional number on the left-hand side $(\tilde{P} - \frac{1}{L}\int_0^L \tilde{P}dx')D/Eh$, represents the ratio of the force produced by pressure acting on a PDMS film to tensile stiffness of the film. Equation (4) indicates that the geometrical indexes on the right-hand sides ($r_{\theta,\emptyset}^*$, $\varepsilon_{\theta,\emptyset}$) are determined by $(\tilde{P} - \frac{1}{L}\int_0^L \tilde{P}dx')D/Eh$, if the equation has a unique solution according to $(\tilde{P} - \frac{1}{L}\int_0^L \tilde{P}dx')D/Eh$. The $\tilde{P} - \frac{1}{L}\int_0^L \tilde{P}dx'$ distribution on the whole film can be normalized with a factor $\Delta\tilde{P}_{\mathrm{film}}$ ($=(1/L)\int_0^L |\tilde{P} - (1/L)\int_0^L \tilde{P}dx'|dx'$), which represents the magnitude of pressure nonuniformity. The normalized pressure distribution exhibits a self-similar profile along the film, regardless of the flow rate as shown in Appendix B.

The variations of mean strain ($\bar{\varepsilon}$) in pulsating cycles for all cases converges with respect to $\Delta\tilde{P}_{\mathrm{film}}D/(Eh)$ as expected in the above analysis [Fig. 3(a)]. The mean stress ($\bar{\sigma}$) acting on each film can be approximately estimated to be $0 \sim 11\,\mathrm{kPa}$ when we apply the value of $\bar{\varepsilon}$ to the above-mentioned Hooke's law with an assumption of $\overline{\varepsilon_\theta} \approx \overline{\varepsilon_\emptyset}$. The estimated $\bar{\sigma}$ values are comparable with the previous results obtained through fluid-structure interaction analysis using numerical simulation, although the maximum stress in the previous results was increased to the order of $10^2\,\mathrm{kPa}$ at a specific location [17,38]. Spatial distribution of stress and the maximum stress value are required to correlate them with stenosis rupture. However, the spatial distribution of stress is hard to be obtained for the present stenosis models. Distinguishable marks or special tracer particles need to be embedded in the fibrous cap-mimicking films to measure the local strain and stress distribution [39,40]. In the present study, we only used the mean stress values, which can be evaluated from length variation of the film, to focus on the effects of flow condition and fibrous cap thickness on stress.
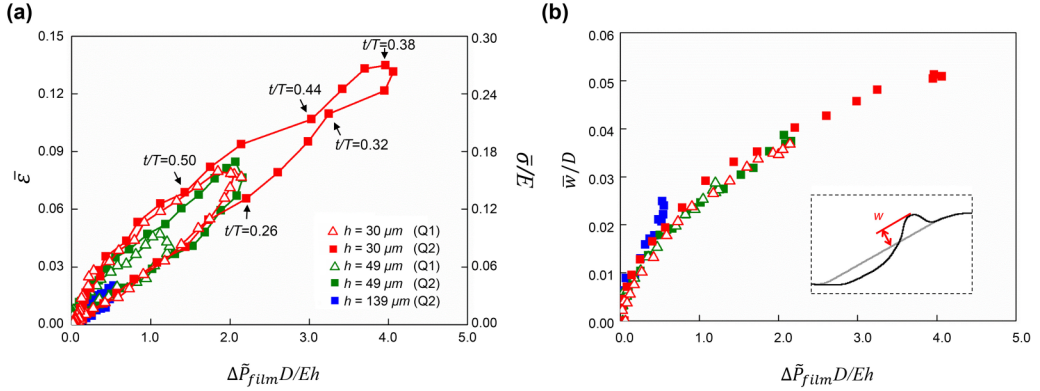
FIG. 3. Normal strain, stress, and deflection of the PDMS films. (a) Hysteresis loops of mean normal strain ($\bar{\varepsilon}$) of the PDMS films at the center plane according to $\Delta\tilde{P}_{\text{film}}D/(Eh)$, where $\Delta\tilde{P}_{\text{film}}$ indicates the pressure nonuniformity factor. The nonuniformity of pressure acting on each film results from pressure gradient, as illustrated in Fig. 2(d). The right axis represents corresponding mean stresses over Young's modulus ($\bar{\sigma}/E$). (b) Variations of the nondimensionalized deflection ($\bar{w}/D$) according to $\Delta\tilde{P}_{\text{film}}D/(Eh)$. The results for five different cases at acceleration phase in the range of $0.02 \leqslant t/T \leqslant 0.38$ are only represented.

The value of $\bar{\varepsilon}$ and $\bar{\sigma}/E$ increase and decrease according to $\Delta\tilde{P}_{\text{film}}D/(Eh)$ in the acceleration and deceleration phases, respectively, as shown in Fig. 3(a). However, the corresponding values for the acceleration and deceleration phases do not converge and exhibit hysteresis behavior. The hysteresis can result from the inertia effect of the film and inequality of the internal pressure in a lipid pool ($\tilde{P}_i$), which is not considered in Eq. (3). The inertial force of the film is evaluated by calculating the acceleration of film deflection (w) in the y' direction (see Appendix C). The maximum inertial force is obtained near the maximum flow rate phase ($t/T = 0.038$), where the relationship between the mean strain $\bar{\varepsilon}$ and $\Delta\tilde{P}_{\text{film}}D/(Eh)$ starts to deviate from the converged trend. However, the inertial force on the film per volume ($\rho_{\text{film}}\delta^2 w/\delta t^2 = A1$) is much smaller than the pressure load ($P - \frac{1}{L}\int_0^L P dx')/(h = A2)$ in Eq. (3) ($A1/A2 < 10^{-2}$). This relatively small inertial force of the film compared to the pressure load is attributed to a small ratio of the inertial forces of the film to the flow [$(\rho_{\text{film}}\delta^2 w/\delta t^2)/(\rho\delta^2\tilde{U}_b/\delta t^2 < 10^{-2})$]. This condition implies that the hysteresis in the strain loop is mainly affected by the inequality of $\tilde{P}_i$ in the lipid pool. The inequality of $\tilde{P}_i$ comes from flow inside the lipid pool, which is induced by the film movement. Although flow analysis is not conducted inside of the lipid pool in the present study, we can expect the inequality of $\tilde{P}_i$ has the maximum value near $t/T = 0.038$ when the inertial force of the film is maximized. The variation of normalized mean deflection ($\bar{w}/D$) at acceleration phase ($0.02 \leqslant t/T \leqslant 0.38$) for all cases also converges according to $\Delta\tilde{P}_{\text{film}}D/(Eh)$ as shown in Fig. 3(b). The converged outcomes result from the geometrical similarity according to $\Delta\tilde{P}_{\text{film}}D/(Eh)$, as expected by Eq. (4). Converged results in Fig. 3 indicate that $\Delta\tilde{P}_{\text{film}}D/(Eh)$ can be applied to estimate the stress acting on the fibrous cap and deflection. However, the value of $\tilde{P}_{\text{film}}$, which can be calculated from pressure distribution, is difficult to obtain from patients in the hospital.

Red squares in Fig. 4(a) represent the relationship between $\Delta\tilde{P}_{\text{film}}$ and the dynamic pressure of the flow ($\rho\tilde{U}_b^2/2$) in the acceleration phase ($0.02 \leqslant t/T \leqslant 0.38$). The value of $\tilde{U}_b$ indicates mean velocity for inlet flow in each phase. The relationship shows that the value of $\Delta\tilde{P}_{\text{film}}$ linearly increases with $\rho\tilde{U}_b^2/2$. To estimate the main reason for the linear relationship, we compare the relative contributions of each budget terms in the following unsteady Reynolds-averaged Navier-Stokes (RANS) equation for the $\Delta\tilde{P}_{\text{film}}$ [41].

$$\frac{\partial \tilde{P}}{\partial x_i} = -\rho \frac{\partial \tilde{u}_i}{\partial t} - \rho \frac{\partial}{\partial x_i}\left(\frac{\tilde{u}_j \tilde{u}_j}{2}\right) + \rho\varepsilon_{ijk}\tilde{u}_j\tilde{w}_k + \mu \frac{\delta^2 \tilde{u}_i}{\partial x_j \partial x_j} - \rho \frac{\partial}{\partial x_j}(\widetilde{u_i' u_j'}). \tag{5}$$
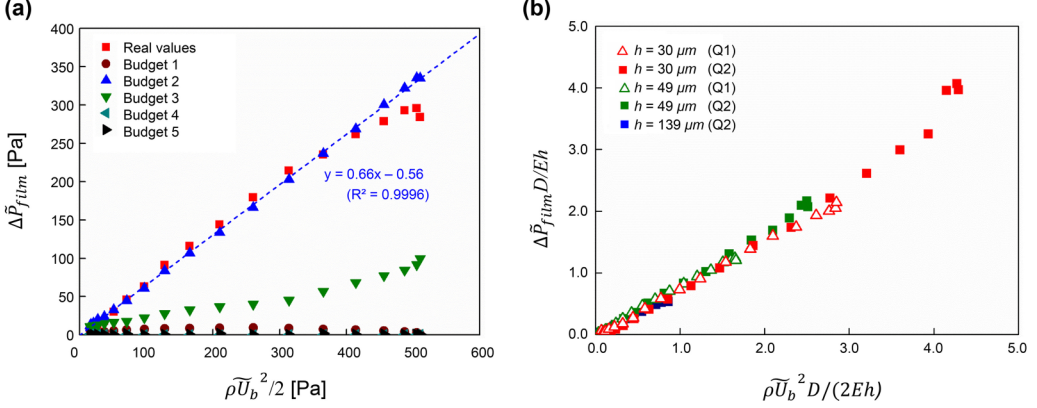
FIG. 4. Relationship between the pressure nonuniformity and flow velocity. (a) Contribution of each budget term in the unsteady RANS equation [Eq. (5)] for pressure nonuniformity factor ($\Delta\tilde{P}_{\text{film}}$) according to the dynamic pressure of the flow ($\rho\widetilde{U}_b^2/2$) at acceleration phase ($0.02 \leqslant t/T \leqslant 0.38$). Real values of $\Delta\tilde{P}_{\text{film}}$ (red square) are calculated by considering all budget terms in Eq. (5). A linear regression line for the result of Budget 2 is represented as a blue dashed line. (b) Relationship between $\Delta\tilde{P}_{\text{film}}D/(Eh)$ and $\widetilde{\rho U_b}^2 D/(2Eh)$.

Each contribution can be compared by calculating $\Delta\tilde{P}_{\text{film}}$ from each static pressure field when one of the right-hand side terms is only considered for calculating $\partial\tilde{P}/\partial x_i$. Budget 2 $[\rho\frac{\partial}{\partial x_i}(\frac{\widetilde{u_j}\widetilde{u_j}}{2})]$ represents the gradient of kinetic energy per volume. Its contribution is higher than those of other terms as shown in Fig. 4(a). The dominance of Budget 2 allows the use of the Bernoulli equation [41]. Hence, $\Delta\tilde{P}_{\text{film}}$ is linearly proportional to $\rho\widetilde{U}_b^2/2$ in the acceleration phase. Figure 4(b) shows variations of $\Delta\tilde{P}_{\text{film}}D/(Eh)$ according to $\rho\widetilde{U}_b^2 D/(2Eh)$ for all cases are converged. The value of $D/(Eh)$ should be multiplied for the two indexes in Fig. 4(a) to consider the effect of shape change according to the $\Delta\tilde{P}_{\text{film}}D/(Eh)$. The linear relationship between $\Delta\tilde{P}_{\text{film}}$ and $\rho\widetilde{U}_b^2/2$ cannot be applied to the deceleration phase because the flow separation in the front side of the stenosis changes the streamlines (see Appendix D).

Based on the linear relationship between $\Delta\tilde{P}_{\text{film}}$ and $\rho\widetilde{U}_b^2/2$, the phase-averaged pressure ($\tilde{P}$) in Eq. (4) was nondimensionalized using $\rho\widetilde{U}_b^2/2$ as follows:

$$\frac{\rho\widetilde{U}_b^2 D}{2Eh}\left(\tilde{P}^* - \frac{1}{L^*}\int_0^{L^*}\tilde{P}^* dx'^*\right) = -\frac{1}{1-\nu^2}\left(\frac{\varepsilon_\theta + \nu\varepsilon_\emptyset}{r_\theta^*} + \frac{\varepsilon_\emptyset + \nu\varepsilon_\theta}{r_\emptyset^*}\right) + \frac{K}{L^*(1-\nu^2)}. \quad (6)$$

The nondimensional number, $\rho\widetilde{U}_b^2 D/(2Eh)$, on the left-hand side represents the ratio of the flow induced inertial force on the film to tensile stiffness of the film. The number has a similar form with the Cauchy number $\{(\rho U^2 D^3/(Eh^3)\}$ which characterizes the elastic bending of a plate by flow induced inertial forces [42,43]. The Cauchy number utilizes bending stiffness ($\sim Eh^3$) instead of tensile stiffness ($\sim Eh$). The nondimensionalized pressure distribution ($\tilde{P}^* - \frac{1}{L^*}\int_0^{L^*}\tilde{P}^* dx'^*$) on the film is determined by $\rho\widetilde{U}_b^2 D/(2Eh)$ due to the self-similarity of pressure profiles along the film (Appendix B) and the linear relationship between $\Delta\tilde{P}_{\text{film}}$ and $\rho\widetilde{U}_b^2/2$. Equation (6) indicates that the geometrical indexes on the right-hand sides ($r_{\theta,\emptyset}^*$, $\varepsilon_{\theta,\emptyset}$) is determined by the $\rho\widetilde{U}_b^2 D/(2Eh)$, if the equation has a unique solution according to $\rho\widetilde{U}_b^2 D/(2Eh)$.

The variations of $\bar{\varepsilon}$ and $\bar{\sigma}/E$ according to $\rho\widetilde{U}_b^2 D/(2Eh)$ converge at acceleration phase ($0.02 \leqslant t/T \leqslant 0.38$) as shown in Fig. 5(a), because of the results in Fig. 3(a) and converged relationship between $\Delta\tilde{P}_{\text{film}}D/(Eh)$ and $\rho\widetilde{U}_b^2 D/(2Eh)$ in Fig. 4(b). These results denote that the
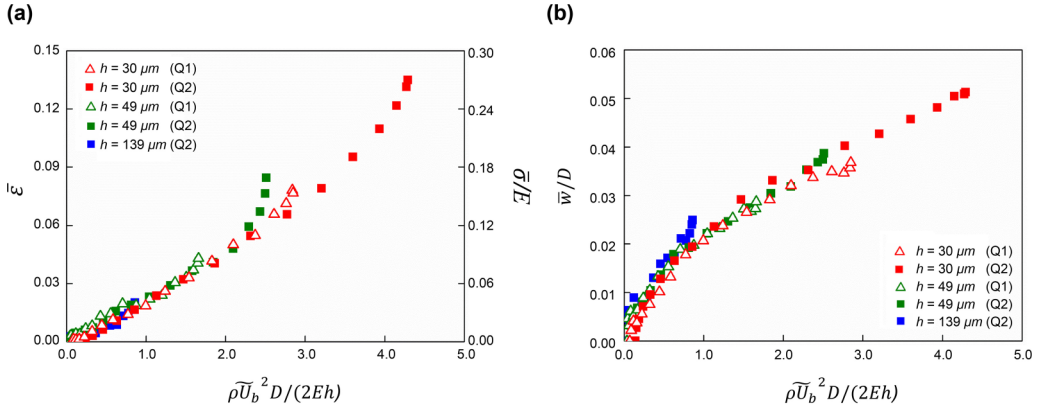
FIG. 5. (a) Variations of the mean normal strain ($\bar{\varepsilon}$) and the mean normal stress over Young's modulus ($\bar{\sigma}/E$) according to $\rho\widetilde{U}_b^2 D/(2Eh)$. The results for five different cases at acceleration phase in the range of $0.02 \leqslant t/T \leqslant 0.38$ are compared. (b) Variations of the nondimensionalized deflection ($\bar{w}/D$) according to $\rho\widetilde{U}_b^2 D/(2Eh)$ for five different cases at acceleration phase ($0.02 \leqslant t/T \leqslant 0.38$) .

stress acting on fibrous caps can be roughly anticipated by measuring the flow rate and fibrous cap thickness. The variations of deflection ($\bar{w}/D$) are also converged according to $\rho\widetilde{U}_b^2 D/(2Eh)$, as shown in Fig. 5(b).

The above results are obtained for the present stenosis models of which the conduit diameters (D) are 10 mm. To examine the results for various vessel sizes, the term $\rho\widetilde{U}_b^2 D/(2Eh)$ in Eq. (6) can be expressed as $\rho\nu^2 Re'^2/(2EhD)$ by using the characteristic Reynolds number ($Re' = \widetilde{U}_b D/\nu$). This result indicates that the values of $\bar{\varepsilon}$ and $\bar{\sigma}$ are inversely proportional to the geometrical size of the vessel ($\sim 1/D$) in consideration of dynamic similarity and the roughly linear relationship illustrated in Fig. 5. We can anticipate larger stress ($\bar{\sigma}$) in carotid and coronary arteries comparing to $\bar{\sigma}$ in the present model because the diameter of the arteries are usually smaller than 10 mm [44,45].

C. Diagnosis index related with jet-flow angle

In this section, we discuss the effects of stenotic deformation on the flow around the stenosis. When the conduit area decreases in the region in front of the stenosis, a high-speed jet flow is formed at the throat of the stenosis ($x/D = 0$) as shown in a flow visualization result [Fig. 1(d)]. The velocity profile of the jet flow is commonly utilized to diagnose the severity of stenosis or to check the malfunction of aortic valve [46]. The jet flow influences the wall shear stress distribution in the downstream of the stenosis and the pressure drop across the stenosis [47–49]. The phase-averaged wall-normal velocity ($\tilde{V}/U_m$) profiles in the region near the throat of the stenosis ($x/D = 0$) were compared in Figs. 6(a) and 6(b). At the slow flow phase ($t/T = 0.2$), the $\tilde{V}/U_m$ magnitude for the three different deformable stenosis models are similar to the value for the flat-rigid stenosis model because the upstream shape of the stenosis are similar. However, the wall-normal velocities of the models become discernible at high-speed flow phase ($t/T = 0.38$) as illustrated in Fig. 6(b). The deformable stenosis models with thin films have low $\tilde{V}/U_m$ values because the high deflection ($\bar{w}$) of the film decreases the geometrical slope in the region near the stenosis throat ($-0.3 \leqslant x/D \leqslant -0.2$) as shown in Fig. 2(c). The low $\tilde{V}/U_m$ of thin films induces a jet flow with small angle ($\bar{\alpha}$). $\bar{\alpha}$ indicates the mean angle of the velocity vector near the stenosis throat as represented in Fig. 6(c). The angle of velocity vectors from bottom surface to center of the conduit are averaged at a specific x position to calculate $\bar{\alpha}$.

Figure 6(c) shows the variations of jet-flow angle at the throat ($x/D = 0$) according to t/T. The jet-flow angle of each model is temporally decreased near $t/T = 0.1$ in common due to large
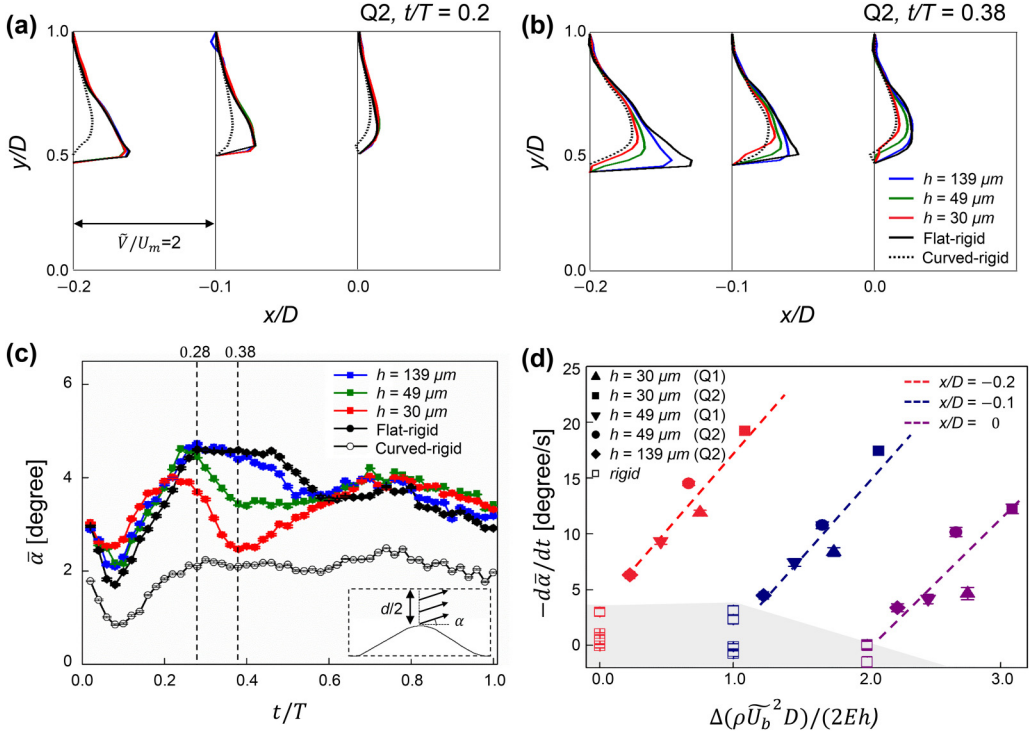
FIG. 6. Variations of phase-averaged wall-normal velocity profile ($\tilde{V}$) normalized by the time-averaged bulk velocity (U_m) in the region near the throat of the stenosis ($-0.2 \leqslant x/D \leqslant 0$) at (a) $t/T = 0.2$ and (b) $t/T = 0.38$ for Q2 flow condition. (c) Variations of the mean jet-flow angles ($\bar{\alpha}$) at the throat of the stenosis ($x/D = 0$) for Q2 flow condition. (d) Mean slope $-d\bar{\alpha}/dt$ values in the region of $0.28 \leqslant t/T \leqslant 0.38$ in Fig. 6(c) is calculated for each stenosis model. Variations of the index $-d\bar{\alpha}/dt$ according to $\Delta(\rho\widetilde{U}_b^2 D)/(2Eh)$ $[=(\rho\widetilde{U}_b^2 D)/(2Eh)_{t/T=0.38} - (\rho\widetilde{U}_b^2 D)/(2Eh)_{t/T=0.28}]$. The open squares in the gray zone denote the data obtained from rigid stenosis models. Error bars in (c) and (d) denote the standard deviation of the data acquired at a neighbored x position ($\Delta x/D = 0.02$). Dashed lines are guides to the eye. Note: Data for $x/D = 0.1$ and $x/D = 0$ are moved in parallel along the x axis with increments of 1.0 and 2.0, respectively, to avoid overlapping.

recirculation region developed in the previous cycle as represented in previous results [50]. In the deceleration phase near $t/T = 0.7$, the opposite phenomena occur in all models. This phenomenon might be affected by the adverse pressure gradient formed in the downstream flow [51]. We focused on the jet-angle variations at high-speed flow phases, in which the effect of initial flow condition and deceleration is minimized. For the two different rigid models, the jet-flow angle ($\bar{\alpha}$) is sustained in the region ($0.28 \leqslant t/T \leqslant 0.38$), although the magnitudes of the two models are distinctive due to different stenotic shapes. However, the jet-flow angle decreases gradually in the region of the deformable models. Especially, the angle is sharply decreased when the film thickness decreases. The large variation of jet angle in the models with thin films is attributed to the large variation of the upstream stenosis shape. The mean variation of jet-flow angle ($-d\bar{\alpha}/dt$) in the region is calculated for each model, and the results are compared in Fig. 6(d). The value increases when the film thickness decreases and the flow rate increases, regardless of the measurement location ($-0.2 \leqslant x/D \leqslant 0$). The values for the rigid stenosis models (open squares) are smaller than those for the deformable stenosis models. When the $-d\bar{\alpha}/dt$ values are plotted according to $\Delta(\rho\widetilde{U}_b^2 D)/(2Eh)$ $[= (\rho\widetilde{U}_b^2 D)/(2Eh)_{t/T=0.38} - (\rho\widetilde{U}_b^2 D)/(2Eh)_{t/T=0.28}]$, positive relationships

between the two parameters are obtained. The increased $\Delta(\rho\widetilde{U}_b^2 D)/(2Eh)$ induces large variation in deflection ($\bar{w}$) as shown in Fig. 5(b). The large deflection ultimately results in high values of $-d\bar{\alpha}/dt$. The positive relationship between $-d\bar{\alpha}/dt$ and $\Delta(\rho\widetilde{U}_b^2 D)/(2Eh)$ is evident at the location of $x/D = -2$ compared with $x/D = 0$ because the effect of film deflection on $\tilde{V}/U_m$ decreases when the flow goes downstream as represented in Fig. 6(b). These results indicate that the variation of jet-flow angle can be utilized to distinguish a deformable stenosis from a rigid one and to estimate normal stress acting on fibrous cap. The jet-flow angle ($\bar{\alpha}$) and the phase-averaged bulk velocity ($\widetilde{U}_b$) can be measured by any noninvasive flow measurement techniques, including spectral Doppler ultrasound [52], ultrasound speckle image velocimetry [53], phase-contrast magnetic resonance imaging [54], and vector flow-imaging technique [55].

We tested three deformable stenosis models having flexible film on the upstream side. Clinical studies already reported that the rupture usually occurs in the upstream side of stenosis [56,57]. Kume *et al.* [6] clinically observed the deformation of a patient's stenosis which has a similar shape with our stenosis models. Although various stenosis shapes need to be considered to suggest a universal index, the present models with flexible films in the upstream side can be considered as a representative model of rupturable stenoses.

In our previous study, a deformable stenosis model having flexible films on the both upstream and downstream side is tested [58]. Jet-angle variation induced by stenosis deformation, representative jet characteristics observed in the present models, was also observed in the previous model, although the study was conducted in steady flow condition.

However, the deformation and resultant jet-velocity profiles need to be examined for various shaped models and the proposed diagnosis index should be checked by clinical data to validate its universality in the future.

IV. CONCLUDING REMARKS

In this study, $\Delta(\rho\widetilde{U}_b^2 D)/(2Eh)$ is found to be a determinant index for assessing the mean deflection ($\bar{w}$) of the fibrous caps (PDMS films) and the mean normal stress ($\tilde{\sigma}$) acting on the caps. In addition, we found another index $-d\bar{\alpha}/dt$ which can be effectively used to detect a deformable stenosis and anticipate mechanical stress acting on the fibrous caps. The usefulness of the two proposed indexes, $\Delta(\rho\widetilde{U}_b^2 D)/(2Eh)$ and $-\frac{d\alpha}{dt}$, must be validated in complicated geometries and various flow conditions to be applied for patients in clinical practice.

ACKNOWLEDGMENT

APPENDIX A: CONFIGURATION OF A DEFORMABLE STENOSIS MODEL

The deformable stenosis models have eccentric configuration, which can be expressed by the following equation:

$$\frac{d(x)}{D} = 1 - \frac{45}{200}\left[1 + \cos\left(\frac{x\pi}{D}\right)\right], \quad 0 \leqslant x/D \leqslant 1, \tag{A1}$$

$$\frac{c(x)}{D} = 1 - \frac{d(x)}{2D}, \qquad 0 \leqslant x/D \leqslant 1, \tag{A2}$$

where d is the circular conduit diameter of the stenosis, c represents the y-directional position of the circular center, and D is the vessel diameter ($D = 10$ mm). The stenotic geometry expressed with the above expression is similar to that of previous studies [59,60]. The cross section of the conduit
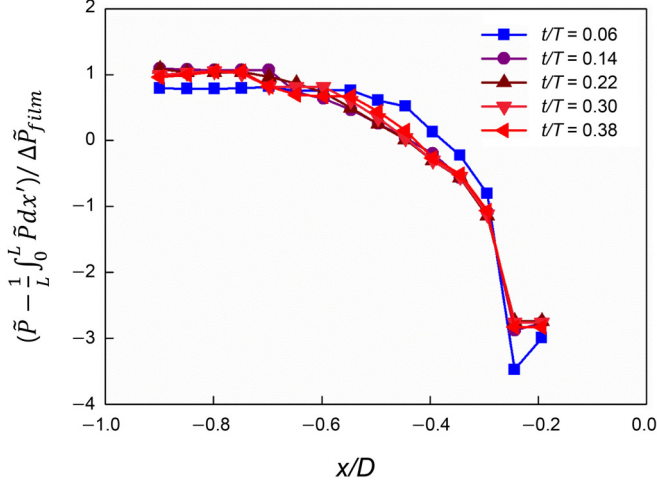
FIG. 7. Variations of the normalized pressure $[(\tilde{P} - \frac{1}{L}\int_0^L \tilde{P}dx')/\Delta\tilde{P}_{\text{film}}]$ acting on the upstream side of the stenosis $(-0.9x/D < -0.2)$ according to x position. The results obtained from a flat-rigid stenosis model at five different phases are represented for comparison. The range of x position $(-0.9 < x/D < -0.2)$ corresponds to the location of PDMS films in the deformable stenosis models tested in this study.

in front of the stenosis throat $(-1 \leqslant x/D \leqslant 0)$ has a shape of circular arc that passes through the following three points.

The location of the first point is as follows:

$$(x, y, z) = (x, D, 0), \quad -1 \leqslant x/D \leqslant 0 \tag{A3}$$

The locations of the other points are as follows:

$$(x, y, z) = \left(x, \frac{45D}{200}\left[1 + \cos\left(\frac{x\pi}{D}\right)\right], Z\right), \tag{A4}$$

where

$$Z = \pm 2(x+1)D, \quad -1 \leqslant x/D \leqslant -0.9, \tag{A5}$$

$$Z = \pm 0.2D, \quad -0.9 \leqslant x/D \leqslant -0.2, \tag{A6}$$

$$Z = \mp x, \quad -0.2 \leqslant x/D \leqslant 0. \tag{A7}$$

APPENDIX B: SELF-SIMILARITY OF THE MEASURED PRESSURE PROFILES

The phase-averaged pressure distribution is subtracted by the mean pressure value along the film $(\frac{1}{L}\int_0^L \tilde{P}dx')$ and normalized by the pressure nonuniformity factor, $\Delta\tilde{P}_{\text{film}}$ (see Fig. 7). The normalized pressure distributions at five different phases are converged, except at the phase of small flow rate $(t/T = 0.06)$. The converged pressure distribution is related with the self-similar velocity profile near the stenosis, except at $t/T = 0.06$.

APPENDIX C: EFFECTS OF INERTIAL FORCE

The inertial force per volume of each PDMS film is approximately estimated by calculating the acceleration of deflection in the y' direction, as shown in Fig. 2(c) (see Fig. 8). Positive and negative
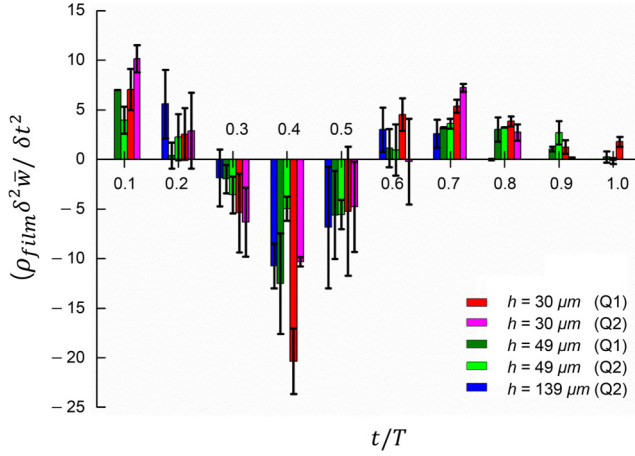
FIG. 8. Variations of inertial force per volume ($\rho_{film}\delta^2\bar{w}/\delta t^2$) of the PDMS films according to t/T. Error bars denote the standard deviation of the data obtained from neighbored t/T with an interval of $\Delta t/T = 0.1$.

values of the inertial force represent the acceleration and deceleration of the film movement in the y' direction, respectively. The magnitude of the inertial force has the maximum value near the phase of maximum flow rate ($t/T = 0.038$).

APPENDIX D: VARIATIONS OF PRESSURE NONUNIFORMITY FACTOR ACCORDING TO THE SQUARE OF PHASE-AVERAGED BULK VELOCITY AT DECELERATION PHASE

Linear relationship between $\Delta\tilde{P}_{film}$ and $\rho\widetilde{U}_b^2/2$ established at the acceleration phase ($0.02 \leqslant t/T \leqslant 0.38$) is not observed in the deceleration phase ($0.40 \leqslant t/T \leqslant 1.00$), as marked by red squares in Fig. 9(a). The recirculating flow in Fig. 9(b) is induced by adverse pressure gradient at the upstream side of the stenosis in the deceleration phase [61].
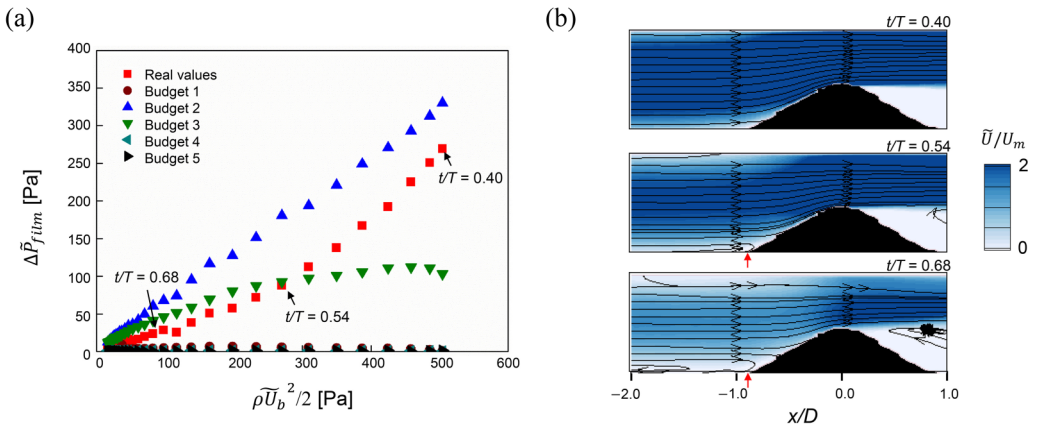

FIG. 9. (a) Contribution of each budget term in the unsteady RANS equation [Eq. (5)] for pressure nonuniformity factor ($\Delta\tilde{P}_{film}$) according to the dynamic pressure of the flow ($\rho\widetilde{U}_b^2/2$) at deceleration phase ($0.40 \leqslant t/T \leqslant 1.00$). (b) Contours of the phase-averaged axial velocity normalized by the time-averaged bulk velocity ($\tilde{U}/U_m$) around the flat-rigid stenosis model at $t/T = 0.40$, 0.54, and 0.68 under Q2 flow condition. Recirculating flow is formed in the upstream side of the stenosis as marked by red arrows.

[1] M. Naghavi *et al.*, From vulnerable plaque to vulnerable patient: A call for new definitions and risk assessment strategies: Part II, Circulation **108**, 1772 (2003).

[2] C. J. Slager, J. J. Wentzel, F. J. Gijsen, J. C. Schuurbiers, A. C. van der Wal, A. F. van der Steen, and P. W. Serruys, The role of shear stress in the generation of rupture-prone vulnerable plaques, Nat. Clin. Pract. Cardiovasc. Med. **2**, 401 (2005).

[3] S. Carr, A. Farb, W. H. Pearce, R. Virmani, and J. S. Yao, Atherosclerotic plaque rupture in symptomatic carotid artery stenosis, J. Vasc. Surg. **23**, 755 (1996).

[4] T. Funaki, K. Iihara, S. Miyamoto, K. Nagatsuka, T. Hishikawa, and H. Ishibashi-Ueda, Histologic characterization of mobile and nonmobile carotid plaques detected with ultrasound imaging, J. Vasc. Surg. **53**, 977 (2011).

[5] T. Ogata, M. Yasaka, Y. Wakugawa, T. Kitazono, and Y. Okada, Morphological classification of mobile plaques and their association with early recurrence of stroke, Cerebrovasc. Dis. **30**, 606 (2010).

[6] S. Kume, S. Hama, K. Yamane, S. Wada, T. Nishida, and K. Kurisu, Vulnerable carotid arterial plaque causing repeated ischemic stroke can be detected with B-mode ultrasonography as a mobile component: Jellyfish sign, Neurosurg. Rev. **33**, 419 (2010).

[7] S. Meairs and M. Hennerici, Four-dimensional ultrasonographic characterization of plaque surface motion in patients with symptomatic and asymptomatic carotid artery stenosis, Stroke **30**, 1807 (1999).

[8] X. Z. Huang, Z. Y. Wang, X. H. Dai, Z. Yun, and M. Zhang, Velocity vector imaging of longitudinal mechanical properties of upstream and downstream shoulders and fibrous cap tops of human carotid atherosclerotic plaque, Echocardiography **30**, 211 (2013).

[9] F. Sharif and R. T. Murphy, Current status of vulnerable plaque detection, Catheter Cardiovasc. Interv. **75**, 135 (2010).

[10] D. Tang, C. Yang, S. Kobayashi, and D. N. Ku, Effect of a lipid pool on stress/strain distributions in stenotic arteries: 3-D fluid-structure interactions (FSI) models, J. Biomech. Eng. **126**, 363 (2004).

[11] G. Choi *et al.*, Coronary artery axial plaque stress and its relationship with lesion geometry: Application of computational fluid dynamics to coronary CT angiography, JACC Cardiovasc. Imaging **8**, 1156 (2015).

[12] S. J. Kang *et al.*, Plaque structural stress assessed by virtual histology-intravascular ultrasound predicts dynamic changes in phenotype and composition of untreated coronary artery lesions, Atherosclerosis **254**, 85 (2016).

[13] Y. Vengrenyuk, S. Carlier, S. Xanthos, L. Cardoso, P. Ganatos, R. Virmani, S. Einav, L. Gilchrist, and S. Weinbaum, A hypothesis for vulnerable plaque rupture due to stress-induced debonding around cellular microcalcifications in thin fibrous caps, Proc. Natl. Acad. Sci. USA **103**, 14678 (2006).

[14] Z. Y. Li, S. P. Howarth, T. Tang, M. J. Graves, J.-U.-K. Im, R. A. Trivedi, P. J. Kirkpatrick, and J. H. Gillard, Structural analysis and magnetic resonance imaging predict plaque vulnerability: A study comparing symptomatic and asymptomatic individuals, J. Vasc. Surg. **45**, 768 (2007).

[15] G. Finet, J. Ohayon, and G. Rioufol, Biomechanical interaction between cap thickness, lipid core composition and blood pressure in vulnerable coronary plaque: Impact on stability or instability, Coronary Artery Dis. **15**, 13 (2004).

[16] A. J. Brown *et al.*, Plaque structural stress estimations improve prediction of future major adverse cardiovascular events after intracoronary imaging, Circ-Cardiovas. Imag. **9**, e004172 (2016).

[17] D. Tang, C. Yang, J. Zheng, P. K. Woodard, J. E. Saffitz, G. A. Sicard, T. K. Pilgram, and C. Yuan, Quantifying effects of plaque structure and material properties on stress distributions in human atherosclerotic plaques using 3D FSI models, J. Biomech. Eng. **127**, 1185 (2005).

[18] J. A. Schaar, C. L. De Korte, F. Mastik, C. Strijder, G. Pasterkamp, E. Boersma, P. W. Serruys, and A. F. Van Der Steen, Characterizing vulnerable plaque features with intravascular elastography, Circulation **108**, 2636 (2003).

[19] C. L. de Korte, A. F. van der Steen, E. I. Cepedes, G. Pasterkamp, S. G. Carlier, F. Mastik, A. H. Schoneveld, P. W. Serruys, and N. Bom, Characterization of plaque components and vulnerability with intravascular ultrasound elastography, Phys. Med. Biol. **45**, 1465 (2000).

[20] J. F. Wenk, P. Papadopoulos, and T. I. Zohdi, Numerical modeling of stress in stenotic arteries with microcalcifications: A micromechanical approximation, J. Biomech. Eng. **132**, 091011 (2010).

[21] L. Cardoso and S. Weinbaum, Changing views of the biomechanics of vulnerable plaque rupture: A review, Ann. Biomed. Eng. **42**, 415 (2014).

[22] P. D. Richardson, M. J. Davies, and G. V. Born, Influence of plaque configuration and stress distribution on fissuring of coronary atherosclerotic plaques, Lancet. **2**, 941 (1989).

[23] A. S. Go *et al.*, On behalf of the American Heart Association statistics committee and stroke statistics subcommittee, Heart disease and stroke statistics—2013 update: A report from the American Heart Association, Circulation **127**, e1 (2013).

[24] J. T. Pham, F. Schellenberger, M. Kappl, and H. J. Butt, From elasticity to capillarity in soft materials indentation, Phys. Rev. Mater. **1**, 015602 (2017).

[25] S. R. Barrett, M. P. Sutcliffe, S. Howarth, Z. Y. Li, and J. H. Gillard, Experimental measurement of the mechanical properties of carotid atherothrombotic plaque fibrous cap, J. Biomech. **42**, 1650 (2009).

[26] R. T. Lee, A. J. Grodzinsky, E. H. Frank, R. D. Kamm, and F. J. Schoen, Structure-dependent dynamic mechanical behavior of fibrous caps from human atherosclerotic plaques, Circulation **83**, 1764 (1991).

[27] M. Y. Yousif, D. W. Holdsworth, and T. L. Poepping, A blood-mimicking fluid for particle image velocimetry with silicone vascular models, Exp. Fluids **50**, 769 (2011).

[28] D. W. Holdsworth, C. J. Norley, R. Frayne, D. A. Steinman, and B. K. Rutt, Characterization of common carotid artery blood-flow waveforms in normal human subjects, Physiol. Meas. **20**, 219 (1999).

[29] X. He and D. N. Ku, Unsteady entrance flow development in a straight tube, J. Biomech. Eng. **116**, 355 (1994).

[30] W. Choi, J. H. Park, H. Byeon, and S. J. Lee, Flow characteristics around a deformable stenosis under pulsatile flow condition, Phys. Fluids **30**, 011902 (2018).

[31] J. O. Dabiri, S. Bose, B. J. Gemmell, S. P. Colin, and J. H. Costello, An algorithm to estimate unsteady and quasi-steady pressure fields from velocity field measurements, J. Exp. Biol. **217**, 331 (2014).

[32] C. J. Kähler, S. Scharnowski, and C. Cierpka, On the uncertainty of digital PIV and PTV near walls, Exp. Fluids **52**, 1641 (2012).

[33] J. Westerweel, On velocity gradients in PIV interrogation, Exp. Fluids **44**, 831 (2008).

[34] W. Choi, H. M. Kim, S. Park, E. Yeom, J. Doh, and S. J. Lee, Variation in wall shear stress in channel networks of zebrafish models, J. R. Soc. Interface **14**, 20160900 (2017).

[35] G. Giuliano, *Superplastic Forming of Advanced Metallic Materials* (Woodhead Publishing Limited, Cambridge, 2011), p. 115.

[36] F. Beer, J. DeWolf, E. R. Johnston Jr, and D. Mazurek, *Mechanics of Materials* (Elsevier, Oxford, 2014).

[37] V. M. Kulik, A. V. Boiko, S. P. Bardakhanov, H. Park, H. H. Chun, and I. Lee, Viscoelastic properties of silicone rubber with admixture of SiO_2 nanoparticles, Mat. Sci. Eng. A-Struct. **528**, 5729 (2011).

[38] D. Tang, C. Yang, S. Mondal, F. Liu, G. Canton, T. S. Hatsukami, and C. Yuan, A negative correlation between human carotid atherosclerotic plaque progression and plaque wall stress: In vivo MRI-based 2D/3D FSI models, J. Biomech. **41**, 727 (2008).

[39] F. Tournoux *et al.*, Estimation of radial strain and rotation using a new algorithm based on speckle tracking, J. Am. Soc. Echocardiogr. **21**, 1168 (2008).

[40] M. McCormick, T. Varghese, X. Wang, C. Mitchell, M. A. Kliewer, and R. J. Dempsey, Methods for robust *in vivo* strain estimation in the carotid artery, Phys. Med. Biol. **57**, 7329 (2012).

[41] P. Kundu, I. Cohen, and D. Dowling, *Fluid Mechanics*, 5th ed. (Elsevier, Amsterdam, 2012).

[42] E. De Langre, Effects of wind on plants, Annu. Rev. Fluid Mech. **40**, 141 (2008).

[43] F. Gosselin, E. De Langre, and B. A. Machado-Almeida, Drag reduction of flexible plates by reconfiguration, J. Fluid Mech. **650**, 319 (2010).

[44] J. Krejza, M. Arkuszewski, S. E. Kasner, J. Weigele, A. Ustymowicz, R. W. Hurst, B. L. Cucchiara, and S. R. Messe, Carotid artery diameter in men and women and the relation to body and neck size, Stroke **37**, 1103 (2006).

[45] J. T. Dodge Jr., B. G. Brown, E. L. Bolson, and H. T. Dodge, Lumen diameter of normal human coronary arteries. Influence of age, sex, anatomic variation, and left ventricular hypertrophy or dilation, Circulation **86**, 232 (1992).

[46] J. Garcia, O. R. Marrufo, A. O. Rodriguez, E. Larose, P. Pibarot, and L. Kadem, Cardiovascular magnetic resonance evaluation of aortic stenosis severity using single plane measurement of effective orifice area, J. Cardiovasc. Magn. Reson. **14**, 23 (2012).

[47] H. Ha, J. Lantz, M. Ziegler, B. Casas, M. Karlsson, P. Dyverfeldt, and T. Ebbers, Estimating the irreversible pressure drop across a stenosis by quantifying turbulence production using 4D Flow MRI, Sci. Rep. **7**, 46618 (2017).

[48] B. J. Jeon, H. J. Chang, Y. H. Yoo, and H. G. Choi, A numerical study on the effect of trapezium stenosis shape on the axisymmetric flow field around stenosis, J. Mech. Sci. Technol. **32**, 2651 (2018).

[49] E. Westein, A. D. van der Meer, M. J. Kuijpers, J.-P. Frimat, A. van den Berg, and J. W. Heemskerk, Atherosclerotic geometries exacerbate pathological thrombus formation poststenosis in a von Willebrand factor-dependent manner, Proc. Natl. Acad. Sci. USA **110**, 1357 (2013).

[50] S. S. Varghese, S. H. Frankel, and P. F. Fischer, Direct numerical simulation of stenotic flows. Part 2. Pulsatile flow, J. Fluid Mech. **582**, 281 (2007).

[51] M. E. Boghosian and K. W. Cassel, A pressure-gradient mechanism for vortex shedding in constricted channels, Phys. Fluids **25**, 123603 (2013).

[52] A. H. Brandt, K. L. Hansen, C. Ewertsen, S. Holbek, J. B. Olesen, R. Moshavegh, C. Thomsen, J. A. Jensen, and M. B. Nielsen, A comparison study of vector velocity, spectral doppler and magnetic resonance of blood flow in the common carotid artery, Ultrasound Med. Biol. **44**, 1751 (2018).

[53] E. Yeom, K. H. Nam, D. G. Paeng, and S. J. Lee, Improvement of ultrasound speckle image velocimetry using image enhancement techniques, Ultrasonics **54**, 205 (2014).

[54] G. B. Kim, H. Ha, J. Kweon, S. J. Lee, Y. H. Kim, D. H. Yang, and N. Kim, Post-stenotic plug-like jet with a vortex ring demonstrated by 4D flow MRI, Magn. Reson. Imaging **34**, 371 (2016).

[55] M. M. Pedersen, M. J. Pihl, P. Haugaard, J. M. Hansen, K. L. Hansen, M. B. Nielsen, and J. A. Jensen, Comparison of real-time in vivo spectral and vector velocity estimation, Ultrasound Med. Biol. **38**, 145 (2012).

[56] J. M. Lee *et al.*, Impact of longitudinal lesion geometry on location of plaque rupture and clinical presentations, JACC: Cardiovasc. Imaging **10**, 677 (2017).

[57] C. Costopoulos, Y. Huang, A. J. Brown, P. A. Calvert, S. P. Hoole, N. E. West, J. H. Gillard, Z. Teng, and M. R. Bennett, Plaque rupture in coronary atherosclerosis is associated with increased plaque structural stress, JACC: Caridovasc. Imaging **10**, 1472 (2017).

[58] W. Choi, S. H. Park, H. K. Huh, and S. J. Lee, Hemodynamic characteristics of flow around a deformable stenosis, J. Biomech. **61**, 216 (2017).

[59] S. S. Varghese, S. H. Frankel, and P. F. Fischer, Direct numerical simulation of stenotic flows. Part 1. Steady flow, J. Fluid Mech. **582**, 253 (2007).

[60] S. A. Ahmed and D. P. Giddens, Velocity measurements in steady flow through axisymmetric stenoses at moderate Reynolds numbers, J. Biomech. **16**, 505 (1983).

[61] J.-P. Mollicone, F. Battista, P. Gualtieri, and C. M. Casciola, Effect of geometry and Reynolds number on the turbulent separated flow behind a bulge in a channel, J. Fluid Mech. **823**, 100 (2017).